Integrated campaign to study the stationary inertial Alfvén wave in the laboratory and space regimes

Integrated campaign to study the stationary inertial Alfvén wave in the laboratory and space regimes

M E Koepke[1], S M Finnegan[1], S Vincena[2], D J Knudsen[3] and C Chaston[4]

[1] Department of Physics, West Virginia University, Morgantown, WV, USA
[2] Department of Physics and Astronomy, University of California, Los Angeles, CA, USA
[3] Department of Physics and Astronomy, University of Calgary, Alberta, Canada
[4] Space Sciences Laboratory, University of California, Berkeley, CA, USA

Abstract

A small, off-axis mesh-anode electrode at one plasma-column end is used to create a paraxial channel of electron current and depleted density in the large plasma device upgrade at UCLA. We show that the on-axis, larger, surrounding-plasma column rotates about its cylindrical axis because a radial electric field is imposed by a multiple-segmented-disc termination electrode on the same end as the mesh-anode electrode. The radial profile of azimuthal velocity is shown to be consistent with predictions of rigid-body rotation. Launched inertial Alfvén waves are shown to concentrate in the off-axis channel of electron current and depleted plasma density. In the absence of launched waves, time varying boundary conditions, or spatially structured boundary conditions, a non-fluctuating, non-traveling pattern in the plasma density is shown to arise spontaneously in the channel, but only in the combined presence of electron current, density depletion, and spontaneously in the channel, cross-field convection (i.e. rotation). These results may be relevant to the stationary Alfvén wave in the inertial regime in space and laboratory plasmas.

(Some figures in this article are in colour only in the electronic version)

1. Introduction

The stationary inertial Alfvén (StIA) wave [1] is a non-fluctuating, non-traveling electromagnetic pattern in perturbed electric field, perturbed magnetic field, perturbed plasma density, perturbed ion flow and perturbed electron flow. This pattern has zero time dependence except for that associated with slowly evolving plasma conditions. The free energy of StIA waves is magnetic-field-aligned (s-direction in figure 1) electron drift energy that overcomes collisional dissipation and collisionless phase mixing. The wave pattern is purely spatial and represents an equilibrium solution analogous to a spatially uniform-driven spatial oscillator.
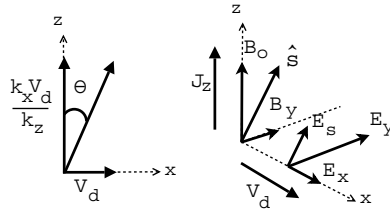
Figure 1. Cartesian geometry of the stationary Alfvén wave model with a depiction of the relevant field and initial flow vectors. For the case shown, $k_x \gg k_y$ and J_z parallel to B_0 (as opposed to antiparallel), the wavevector is angled slightly below and approximately parallel to the vector v_d. The angle in the leftmost coordinate system depicts the orientation of the effective phase velocity vector, as shown, and is approximately zero.

The StIA wave vector is approximately perpendicular to the magnetic field a case for which electron-inertia effects become significant.

To understand the StIA wave, one must transform to the laboratory frame of reference from the plasma-convection frame, rather than transform into a frame that moves at the phase speed, which is non-existent. The historical root of the StIA wave are the papers by Maltsev *et al* [2] and Mallinckrodt and Carlson [3], whereas the historical root of the dispersive inertial Alfvén wave [4] is the paper by Goertz and Boswell [5]. Whereas the dc parallel electric field of the StIA wave may accelerate electrons having speeds on the order of the Alfvén speed ($V_A \equiv B_0/\sqrt{\mu_0 m_i n}$) to higher speeds on the order of 50 times the Alfvén speed, the velocity-space resonance associated with dispersive Alfvén waves inherently limits the maximum attainable electron velocity to speeds on the order of twice the Alfvén speed.

According to the theoretical model of the StIA wave [1], for which the wave vector is antiparallel to the electron $E \times B$ drift (x-direction in figure 1), the perpendicular wavelength is on the order of a few (tens of hundreds) electron inertial lengths, i.e. hundreds of metres (tens of kilometres) across auroral field lines, where the electron inertial length is approximately 10 km. The perturbed magnetic field lies along the y-axis. Knudsen [1], for space conditions, and Finnegan *et al* [6] for laboratory conditions, portray the spatial, pulse-like nature of the perturbed density pattern and the associated electron acceleration that are predicted for the case in which the wave becomes nonlinear.

Because of the purely spatial structure, electrons are accelerated as they drift in the *s*-direction, approximately along the *z*-direction in figure 1. Ground-based imagers would observe a pattern of multiple, parallel, auroral arcs lasting for several minutes or more. The search is for a mechanism of generating enhanced electron energy within long-lived auroral arcs.

With the StIA wave, the presence of plasma drift normal to a current sheet implies an exchange of flux tubes between regions of differing perturbed-magnetic-field energy. The localization of a background current sheet imposes magnetic-field shear $\partial B_y/\partial x$ which implies a gradient in the amount of inductive energy density $B_y^2/2\mu_0$ resident over a region of space. Convection across this gradient leads to a transfer of inductive energy. Thus electron acceleration by the parallel component of the wave electric field on a specific flux tube is powered by inductive energy advecting from a neighboring flux tube.

This laboratory-based space-plasma-physics campaign is intended to contribute toward establishing a complete, all-frequency picture of auroral arcs. The space-plasma physics campaign is a multi-year project designed to emphasize the utility of laboratory experiments to the understanding of space-plasma phenomena [8]. The objective is to experimentally

verify (1) the existence of the StIA wave, (2) the spatial and temporal characteristics of both perturbed parallel electron energy and perturbed plasma density associated with StIA waves, (3) to generalize the StIA wave theory to the laboratory-relevant parameter regime and (4) to predict, via computer simulation, both the observational signature of StIA waves and ramifications of StIA waves for auroral electron precipitation. The short-term experimental goal is to demonstrate electron acceleration in the presence of a StIA wave. The long-term scientific goal is to explore the effects of convection on skin-depth plasma structures in the context of space and laboratory plasmas.

Predictions of the fundamental properties of StIA waves [1] suggest that they may play a role in the formation of discrete auroral arcs and field-line-resonance arcs, within a quasi-static arc structure. The goal of the space-plasma physics campaign is to evaluate this suggestion through laboratory experiment, analytic theory and computer simulation. The original StIA-wave model of uniform plasma convection across field-aligned current sheets has been generalized for laboratory-relevant plasma parameters [6], resulting in the conclusion [7] that significant StIA-wave signatures should be observable in the large plasma device upgrade (LAPD-U) at UCLAs Basic Plasma Science Facility (BAPSF). Here, laboratory results from the West Virginia University Q-Machine [9], using barium-ion plasma, and from LAPD-U [10], using helium-ion plasma, are presented.

Initial experimentation with plasma-rotation-inducing termination electrodes began in May 2006 in the WVU Q-Machine, leading to two designs that, in January 2007, were tested in LAPD. The multiple-segment-disc electrode produced a radial profile of azimuthal velocity that is consistent with predictions of rigid-body rotation. Current-channel experiments in LAPD, in August 2006, showed that launched Alfvén waves in the inertial regime could be concentrated in an off-axis channel of electron current and depleted plasma density. In May 2007, time-stationary structure in the plasma density spontaneously arose when and only when the electron current, density depletion and cross-channel convection coexist during the inertial regime of the LAPD-plasma after-glow decay. Evidence was obtained in September 2007 that the three-dimensional geometry observed in the experiment is consistent with that of the theoretical model. These results are presented in the following sections.

2. Scientific motivation for a laboratory experiment

Arcs are generally elongated in the longitudinal direction with a broad spectrum of cross-arc spatial scale sizes, ranging from less than 100 m to more than 100 km, see [11] and references therein. At least part of the energy carried by arcs is transferred to electrons by wave–particle interactions [12]. For example, this mechanism, among several others, can explain how electron beams are accelerated along auroral magnetic-field lines. Accelerated-electron populations divide into two categories. In the 1–20 keV range, the population's energy is often observed to increase and then decrease as a function of latitude. This signature on an energy spectrum versus time diagram is referred to as an 'inverted-V' event. In the 5–500 eV range, the population is more bursty in its time dependence and more structured in its latitude dependence. Auroral arcs are regions in which the coupling between the magnetosphere, ionosphere and upper atmosphere is enhanced, mediated by streaming particles. Accelerated particles and electromagnetic Poynting flux are responsible for an energy flux in the range 1–100 mW m^{-2}. While auroral arcs exhibit many complex motions, their basic structure often is nearly static over periods of tens of minutes.

Presently, there is no accepted theory that can explain these basic arc properties without presupposing one or more of them (e.g. cross-field length scales, field-aligned current, etc) [13]. For example, electron acceleration to energies of the order of several hundred electron

volt can result if one postulates a magnetospheric source of transient, small-scale Alfvén waves [5, 14–16]. In this scenario, the resulting bursts of accelerated electrons would likely play a role in producing auroral fine structure, meaning transient auroral features with scale size of the order 100–1000 m. Stasiewicz *et al* [17] reviews such small-scale, transient, Alfvén-wave phenomena. On the other hand, most theories of arcs with 10 km scale size require the postulation of a magnetospheric generator. Although the field-line-resonance theory treats arcs as a complete system [18], giving the theory substantially more appeal, the arcs are predicted to oscillate at interhemispheric resonance periods in the range of tens of minutes, a periodic variation in intensity that is rarely observed. Furthermore, the latitudinal elongation of typical arcs would imply oscillation at different field-line resonant periods, which is not evident in the observations. In fact, single quasi-static arcs that each span a latitude range associated with both closed and open magnetic-field lines have been observed, in apparent contradiction to the field-line-resonance interpretation [19]. The frequency dependence of auroral arcs is incompletely understood and is a topic of future fundamental research for space plasmas. For high-frequency arc phenomena, explanations invoke interactions between co-located waves and particles (making modeling straightforward) whereas, for low-frequency arc phenomena, the wave–particle interaction is global since particles have time to travel along the wave and be affected by conditions non-local to the arc (complicating the modeling). Hence, we begin with the model [1] that describes an important role for StIA waves in explaining auroral arcs' frequency dependence. Magnetized plasmas can support non-fluctuating, non-traveling electromagnetic perturbations in an Earth-fixed frame if there is dc magnetic-field-aligned electron current and uniform background plasma convection. Such a stationary pattern should not be confused with standing waves that oscillate in time within a stationary envelope. A stationary wave has no time variation in the Earth-fixed frame. In the plasma-convection frame, there is an apparent propagation speed. The laboratory experiment is designed to subject an off-axis, fixed channel of electron current (and depleted density), created using a small mesh anode or heated, oxide-coated electrode at one plasma-column end, to plasma convection from the plasma column rotating about its cylindrical axis. This rotation is a result of the $\boldsymbol{E} \times \boldsymbol{B}$ drift due to a radial electric field imposed by differentially biased, concentric, annular end segments at the same plasma-column end as the mesh anode.

The two-dimensional Cartesian wave model of the StIA wave developed by Knudsen [1] describes stationary ($\partial/\partial_t = 0$), electromagnetic structure embedded within a cold ($T_e = T_i = 0$), sheet-like ($\partial/\partial_y = 0$) current system. The StIA wave structure is assumed to be oriented obliquely, at a small angle θ, to a uniform background magnetic field ($\hat{z}B_0$) and is supported by uniform plasma flow V_d, due to a convection electric field $E_y = V_d/B_0$, across a magnetic-field-aligned current sheet. As with inertial Alfvén waves, StIA waves carry a cross-field ion polarization current closed by an electron-dominated field-aligned current. The StIA wave-field geometry including initial particle drifts is shown in figure 1. Knudsen's model has been generalized to include the effects of electron and ion collisional resistivity, as well as non-zero thermal pressure [6, 7]. The generalized model describes the stationary Alfvén (StA) wave in both the inertial ($\beta < m_e/m_i$, $k_\perp \lambda_e \sim 1$) and kinetic ($\beta > m_e/m_i$, $k_\perp \rho_i \sim 1$) regimes, and is capable of making predictions of StA wave signatures in laboratory plasma. The set of coupled nonlinear differential equations describing the StA wave [7] are solved numerically for plasma parameters typical of the plasma after-glow (remnant plasma after the main discharge current is terminated) in the LAPD, cf table 1 in Finnegan *et al* [7]. In figure 2, theoretical predictions of StA wave modulated, parallel electron drift (PED) V_{es}/V_{es0} (where V_{es} is the wave enhanced PED and V_{es0} is the initial PED along the s-axis) and background plasma density n/N are plotted with normalized x-position x/λ_e and time, beginning at the termination ($t = 0$) of the plasma discharge current, for initial electron drift $V_{es0} = 0.1V_A$ and
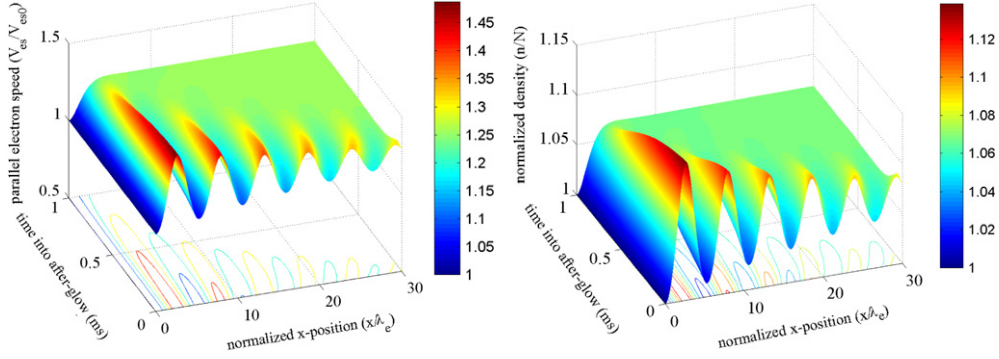
Figure 2. Theoretical predictions of StIA wave perturbations to the PED (left) and background plasma density (right) as a function of time after plasma discharge termination in the LAPD for $V_{es0} = 0.1 V_A$ with $V_{\text{phs}} = 0.5 V_A$.

parallel wave phase speed $V_{\text{phs}} = 0.5 V_A$. For an StIA wave located within a current channel with PED, it is predicted that the density is enhanced and modulated in the direction of the convective flow. Once the discharge current is terminated, the plasma cools and the inertial regime is eventually encountered. Ions cool on the same time scale as the density decay ~ 1 ms, while the electrons cool more rapidly ~ 0.1 ms. The Coulomb collision frequency varies as $T_e^{-3/2}$ with electron temperature. Thus, as the plasma cools, the Coulomb collisional damping of the wave is predicted to increase until the wave is overdamped after $t = 1$ ms resulting in net density enhancement. For initial antiparallel electron drifts (APED), the StA wave is predicted to deplete the background plasma density in the LAPD plasma after-glow [7]. For both PED and APED configurations, the parallel component of StA wave electric field [6],

$$E_s = \frac{m_e}{q_e}[V_d - \theta V_{es}]\frac{\partial V_{es}}{\partial x} + \eta q_e n_e V_{es} - \frac{m_e}{q_e}\theta^2 \frac{V_{Te}^2}{[V_d - \theta V_{es}]}\frac{\partial V_{es}}{\partial x}, \qquad (1)$$

accelerates the background plasma electrons in the magnetic-field-aligned direction. In (1), $\eta = m_e \nu_e / n_e q_e^2$ is the electron collisional resistivity and $V_{Te} = \sqrt{k_B T_e / m_e}$ is the electron thermal speed ($V_{Te}/V_A \sim 0.2\sqrt{m_e/m_i}$ during the first millisecond in the LAPD after-glow plasma). We have assumed, for nearly perpendicularly propagating StA waves, that the balancing of the parallel component of electric field is governed primarily by the parallel electron dynamics. With this assumption, the parallel component of the electric field, equation (1), is calculated from the parallel component of the electron momentum equation. Equation (1) has been written in the form of a generalized Ohm's law and expressed in terms of the parallel electron velocity using relations obtained from the continuity equation as well as the assumption that the parallel current is carried by the electrons. The parallel component of electric field is balanced by electron inertia (first term on right-hand side), parallel resistivity (second term on right-hand side) and parallel electron thermal pressure (last term on right-hand side). For the solutions shown in figure 2, the perpendicular and parallel wavelengths are predicted to be $\lambda_\perp \approx 6.6$ cm and $\lambda_\parallel \approx 550$ cm, respectively. Thus, it should be possible to test the StA wave model by performing experiments in the after-glow plasma of the LAPD.

3. Experimental results—WVUQ

Experiments are performed in the cylindrical, magnetized barium-plasma column (8 cm diameter, 3 m length) of the WVU Q-machine [9] with density 2×10^9 cm³, ion and electron
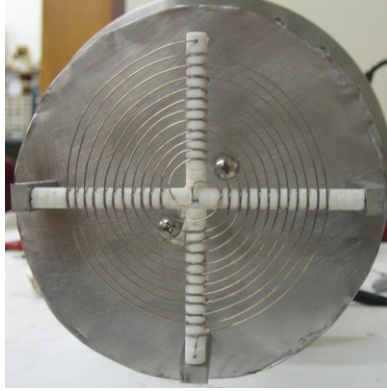
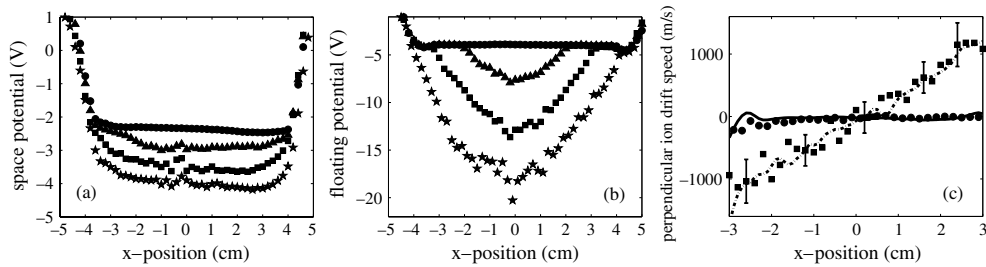**Figure 3.** Photo of the emissive spiral end electrode used in the WVU Q-machine rotation experiments.

Figure 4. The spiral electrode biasing configurations shown are $V_{dc} = 0$ V, $\Delta V = 0$ V ($\bullet$), $V_{dc} = 0$ V, $\Delta V = 13.8$ V ($\blacktriangle$), $V_{dc} = -15$ V, $\Delta V = 13.8$ V ($\blacksquare$) and $V_{dc} = -20$ V, $\Delta V = 13.8$ V ($\star$). (*a*) Measured space potential, (*b*) langmuir probe floating potential and (*c*) perpendicular ion drift speed for rotation experiments on the WVU Q-machine. The diagonal trend in (*c*) shown by the square symbols is opposite to what is expected for an $\boldsymbol{E} \times \boldsymbol{B}$ drift and is interpreted to result from the diamagnetic effects from an emitting spiral wire.

temperatures 0.2 eV, plasma potential -2 V, ion–electron mass ratio 2.5×10^5, base pressure less than 10^{-6} Torr and magnetic field 0.28 T. Laser-induced fluorescence [20] is used to measure one-dimensional velocity distributions. The fluorescent photon flux is proportional to the number of ions at that velocity, within the natural linewidth of the ion (corresponding to $T_i < 0.02$ eV for barium). Sweeping the laser frequency yields the parallel-to-laser-beam velocity distribution $f_0(v)$ for ions. Photons are collected by optics focused on a sub-millimetre spot on the laser line and detected by a photomultiplier tube. Here, x and y refer to orthogonal directions with respect to the z-directed ambient magnetic field.

The goal of the WVU Q-Machine experiment, regarding this project, is to decide on the design of the hardware used to rotate the plasma column about the cylindrical axis. Past experience with multiple segmented disc ionizers [22] and end electrodes [21] provided confidence in that approach. Inspired by the past literature [23] in which a spiral ionizing filament was used, we fabricated a spiral end electrode made out of tungsten, shown in figure 3. The supporting material is alumina (Al_2O_3) and the back plate is stainless steel. The spiral is coiled in a single plane with spacing chosen to be a typical ion gyroradius, which is 5 mm here. Figure 4 shows the performance of the spiral end electrode in influencing the plasma column's radial profile of floating potential and space potential. The space potential is the energy required to bring an electron from infinity into the collected space

charge of the plasma. When an electrostatic probe, inserted into the plasma, is biased at the space potential there is minimal perturbation to the plasma and the particles encounter the surface of the probe by virtue of their thermal motion. The floating potential is the value of applied probe voltage for which the net current collected by the probe is zero. The floating potential can be measured by a probe that is isolated from electrical ground by an infinite resistance ($R \gg R_{\mathrm{plasma}} = (V_{\mathrm{probe}} - V_{\mathrm{plasma}})/I_{\mathrm{probe}}$). Typically, the space potential and floating potential are not equivalent. The space potential and floating potential can be measured almost simultaneously using a swept-bias Langmuir probe. Here, the space potential is approximated to be the inflection point of the current–voltage probe characteristic. Four cases are displayed for the purpose of illustrating control of the azimuthal speed of the plasma column. Note that when the two ends of the spiral filament are grounded, a flat profile is obtained. A similarly flat profile is obtained in the space potential for the other three cases, even though the floating-potential profile appears parabolic for these same three cases. For these three cases, the potential drop between the ends of the spiral filament ΔV were large enough to induce significant electron emission from the spiral filament surface into the plasma. Electron emission was necessary for controlling the radial profile of space potential, but the range of control was too small to produce a parabolic shape in the space-potential profile. The laser-induced fluorescence measurement of V_y versus x, figure 4(c), which indicates a small value of rotational velocity and oppositely directed to the $\boldsymbol{E} \times \boldsymbol{B}$ direction, is interpreted as a demonstration that a diamagnetic drift dominates the ion azimuthal-velocity profile and that a spiral end electrode is undesirable for use in rotating the plasma column. The solid and dashed lines are the flow derived from a combination of $\boldsymbol{E} \times \boldsymbol{B}$ drift inferred from the measured potential profile, and the diamagnetic drift inferred from the measured density profile and the LIF-measured ion temperature, respectively. We note that the profile is indicative of a rigid rotator and, for unknown reasons, the diamagnetic drift is consistent with an elevated ion temperature, specifically $T_i = 8\,\mathrm{eV}$ rather than the typical $T_i = 0.2\,\mathrm{eV}$ normally encountered here and in other Q-machines. The spiral-electrode design was abandoned in favor of a design based on past success with a terminating electrode having multiple concentric segments [21,24].

4. Experimental results—LAPD

The LAPD-U [10] produces a high density, magnetized plasma via a pulsed anode–cathode discharge. The following ranges of pertinent dimensionless parameters are achievable in LAPD-U: number of axial Alfvén wavelengths $0.5 < L/\lambda_{\parallel} < 10$, plasma-$\beta$ $10^{-7} < \beta < 2$, number of particles in a Debye-sphere $10^2 < N_D < 10^6$, magnetization parameter $3 \times 10^{-2} < \omega_{\mathrm{pe}}/\omega_{\mathrm{ce}} < 5 \times 10^4$, ratio of Alfvén speed to electron thermal speed $0.1 < V_A/V_{Te} < 10$. Figure 5 describes pictorially the multiple-segment disc end electrode and the mesh-anode electrode, both of which are installed in the LAPD to produce the $\boldsymbol{E} \times \boldsymbol{B}$ rotation of the helium plasma column and the off-axis current channel, respectively. The experiment is described in terms of a Cartesian coordinate system (x, y, z) whose origin is located at the center of the plasma-producing anode, with the z-axis being aligned with the magnetic-field-aligned cylindrical plasma column. Note that the disc electrode is concentric with the LAPD cylindrical axis and that the mesh-anode electrodes' axis of symmetry is parallel to, but 7.5 cm away from, this cylindrical axis. In this way, $\boldsymbol{E} \times \boldsymbol{B}$ convection, caused by the disc electrode, will be azimuthal and the electron drift, caused by the mesh-anode electrode, will be longitudinal. Figure 6 displays the evidence that the mesh-anode electrode indeed produces a density-depleted channel, implying that the electron drift is confined to this channel, and that the radial profile of longitudinal ion drift is confined to this channel. Figure 7 displays the evidence that the multiple-segment disc electrode indeed produces a parabolic radial profile of space
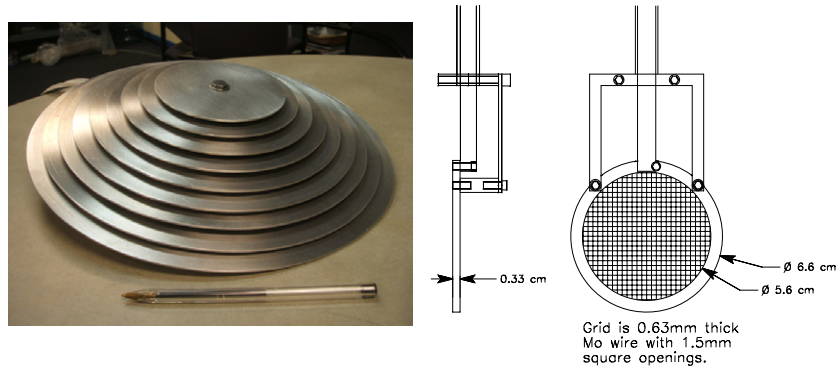
Figure 5. (Left) Picture of the multi-disc electrode (MDE). (Right) Schematic of the mesh anode used to produce the off-axis current channel.
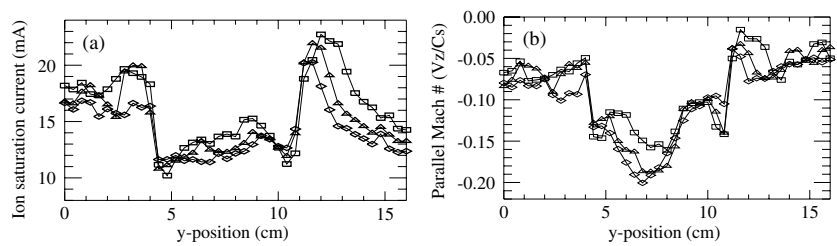

Figure 6. An off-axis (in *y*-direction) current channel (density depletion) (*a*) is created by applying a voltage drop between a copper mesh electrode and the plasma source anode ($\Delta V = 40$ V (diamonds), 60 V (triangles) and 80 V (squares)). The parallel ion drift (*b*) was measured using a mach probe.
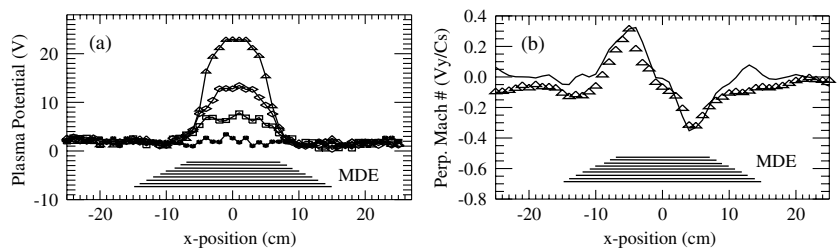

Figure 7. Adjusting the dc potential drop applied across the faces of the MDE, the plasma potential profile (*a*) and hence electric field profile can be varied. $\Delta V_{\mathrm{MDE}} = 0$ V (circles), 50 V (squares), 100 V (diamonds) and 150 V (triangles). In part (*b*), mach probe measurement of perpendicular ion flow (triangles) are shown to be in excellent agreement with the theoretically predicted $V_{\boldsymbol{E} \times \boldsymbol{B}} = -E_x/B_0$ drift (solid line) predicted from the measured space potential profile for $\Delta V_{\mathrm{MDE}} = 150$ V.

potential, implying that the $\boldsymbol{E} \times \boldsymbol{B}$ drift profile is parabolic like, and that the radial profile of the *y*-component of ion velocity agrees with the inferred $\boldsymbol{E} \times \boldsymbol{B}$ drift profile. Figure 8 illustrates, with a three-dimensional plot of Fourier spectral power in a plane perpendicular to the magnetic field, that launched Alfvén waves are confined within an off-axis current channel created by a heated cathode 10 cm in diameter centered at $x = 0$ cm and $y = 20$ cm. The two regions of large spectral power within the current channel represent large perturbed-magnetic-field amplitude. Figure 9 reinforces the identity of the current channel in the plane perpendicular
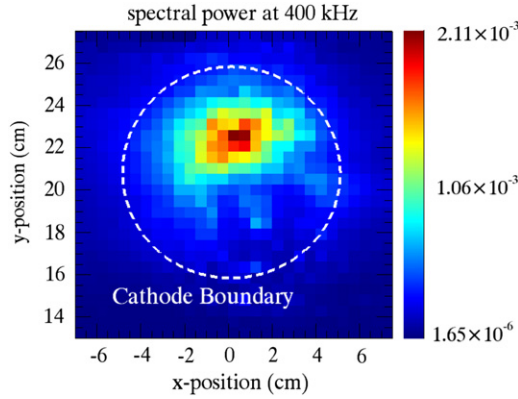
8

Figure 8. Fourier spectral power of an Alfvén wave launched at 400 kHz is localized within an off-axis region of density depletion. Each square super-pixel represents a datum.
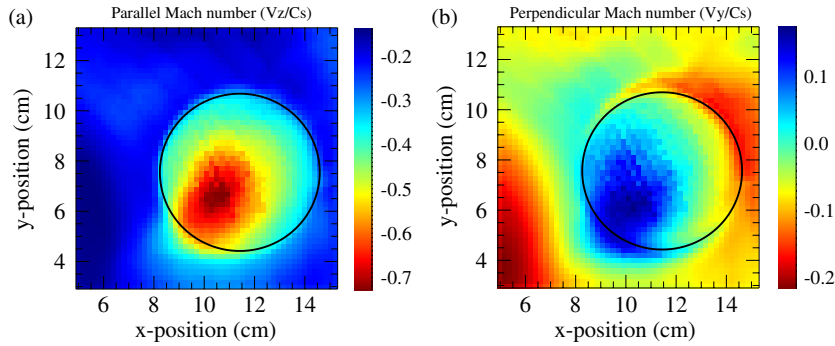

Figure 9. Parallel (*a*) and perpendicular (*b*) ion flow measured with a Mach probe. The dashed–dotted line represents the boundary of the mesh anode. The MDE and mesh anode biases are $\Delta V_{\mathrm{MDE}} = 420$ V and $\Delta V_A = 40$ V, respectively, with $B_0 = 1$ kG. Each square super-pixel represents a datum.

to the magnetic field. In the left panel, the region of longitudinal ion drift is clearly collocated with the region associated with the mesh-anode electrode. The segmented disc electrode is centered on the cylindrical axis of the plasma column. The radius of the innermost disc is 5.2 cm and the radius of the outermost disc is 14.5 cm. In the right panel, the perpendicular ion drift is clearly maximum in the region of the multiple-segment disc electrode. Note that, within the region of the multiple-segment disc electrode, the $E \times B$ drift is evident in the two-dimensional map of the y-component of perpendicular ion drift V_y, except in the region collocated with the region associated with the mesh-anode electrode. In this circular region, the $E \times B$ convection is significantly influenced by the localized potential profile within the off-axis geometry of the channel of density depletion and longitudinal current. This point will be mentioned when describing the geometry of convective flow, structured flow and propagation direction in figure 12. Figure 10 indicates that time-stationary structure is evident in the two-dimensional map of longitudinal ion drift. This structure is confined to the current channel described in figure 6 and appears reproducibly at a specific time in the plasmas after-glow decay, presumably upon the transition from the kinetic Alfvén-wave regime to the inertial Alfvén-wave regime. Note that no launching of waves is occurring in this case. Figure 11(*a*) is a one-dimensional profile of the ion current as a function of the y-position at $x = 11.6$ cm
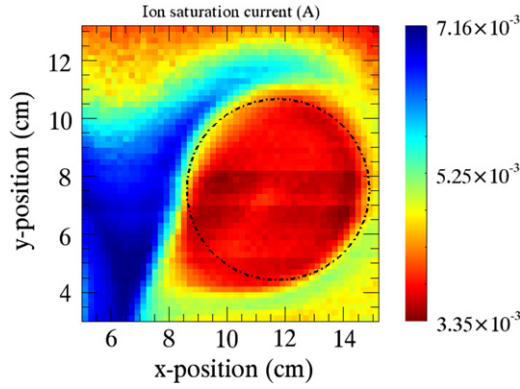
Figure 10. Time-averaged ion saturation current measured on Mach probe collecting surface facing toward the plasma source. The MDE and mesh anode biases are $\Delta V_{\mathrm{MDE}} = 420$ V and $\Delta V_A = 40$ V, respectively, with $B_0 = 1$ kG. Each square super-pixel represents a datum.
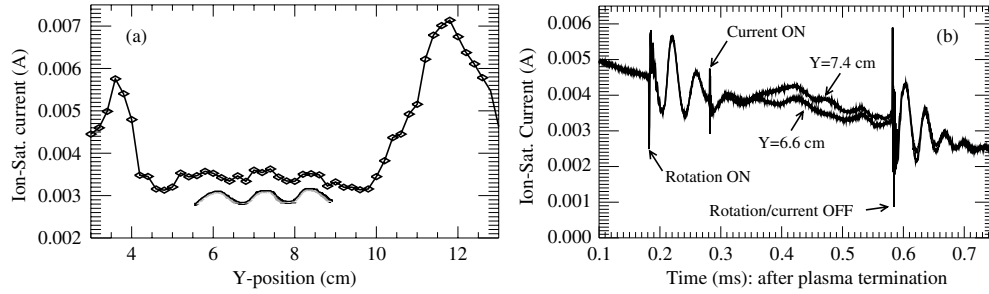

Figure 11. Evidence of a non-fluctuating, non-traveling pattern based on the spatial profile and time evolution of plasma density, as determined by ion saturation current collected by a planar probe. (*a*) Cross-field profile of density, indicating density-depletion channel and evidence of periodic pattern in the density within the channel (smooth line added to guide the eye). (*b*) Evolution of density associated with point $y = 6.6$ cm (bottom line) and $y = 7.4$ cm (top line) for times before, during and after the generation of the electron current channel, indicating negligible density difference except during the time that the StIA wave is expected to exist. The plasma-ionization period ends at $t = 0$ and panel (*a*) corresponds to $t = 0.512$ ms.

and $t = 0.512$ ms after plasma-ionization termination at $t = 0$. The y-axis is chosen because the spatial resolution of the measurement is higher along the y-axis than the resolution oblique to the y-axis. No assumption is made regarding the orientation of the wavevector with respect to the y-axis except that the two are not exactly aligned. Spatially periodic structuring of the ion current (plasma density) is apparent within the boundaries of the current channel. The wavelength of this structure is approximately $\lambda_\perp \approx 1.2$ cm which corresponds to the prediction that $\lambda_\perp$ should be comparable to λ_e. In figure 11(*b*) the ion current measured at spatial points ($x = 11.6$ cm, $y = 6.6$ cm, black line) and ($x = 11.6$ cm, $y = 7.4$ cm, red line) is plotted as a function of time, with plasma-ionization termination serving as the reference time, $t = 0$. These two points are chosen because they are separated by approximately 1/2 wavelength as measured in figure 11(*a*). Note that prior to the initialization of the parallel current, the ion current collected at these two locations is the same. When the parallel current is turned on, the ion current is restructured spatially as seen in figure 11(*a*), decreasing the value of ion current measured at $y = 6.6$ cm (at the trough) relative to the ion current measured at $y = 7.4$ cm (at
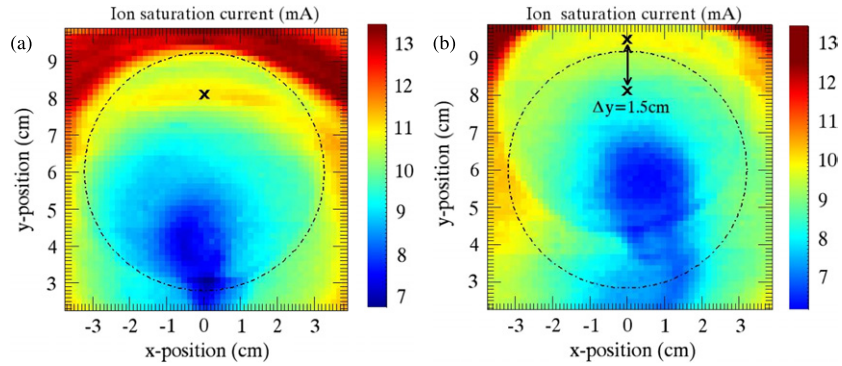
Figure 12. Ion saturation current measured on mach probe collecting surfaces facing toward the plasma source (*a*) at $\Delta z = 2.88$ m and (*b*) at $\Delta z = 1.92$ m (Δz is the axial distance from the mesh anode to the probe). The MDE and mesh-anode biases are $\Delta V_{\text{MDE}} = 80$ V and $\Delta V_A = 40$ V, respectively, with $B_0 = 1$ kG. Each square super-pixel represents a datum.

the crest). The measured ion current at these two spatial locations resumes being the same when both the parallel current and plasma rotation are turned off. The upward shift of structured density from the left panel to the right panel in figure 12 suggests that the propagation angle $\theta = \tan^{-1}(\Delta y / \Delta z)$ associated with the structured density is non-zero, small $\theta \approx 0.015$ rad, and comparable to the square-root of the electron–ion mass ratio $\sqrt{m_e / m_i} = 0.012$. The axial displacement corresponding to the two panels is smaller than one wavelength predicted for the self-excited StIA wave. In this case, a vertically upward component of convective flow was measured using pairs of directionally opposite current-collecting faces, on the x-axis-oriented cylindrical mach probe having six faces around the cylinder's circumference (one pair of faces are magnetic field aligned and two pairs are at plus and minus 45 degrees to that). Although a horizontal component of convective flow is presumed to exist, the probe was not oriented in a way to measure it. Note that ion saturation probe current shown in figures 8 and 9 is measured using one face of the mach probe. Note that this figure has the mesh-anode region at 12 o'clock, as in figure 8, whereas the mesh-anode region in figures 9 and 10 is 1:30 (i.e. 45° upward and to the right).

5. Discussion

The Q-machine result regarding the spiral electrode and previous Q-machine experience with various segmented disc electrodes [21] motivated the use of multi-segment disc electrode in the LAPD-U. The Q-machine results have ramifications on interpreting the value of ion drift velocity in Q-machines that lack the advantage of laser-induced fluorescence measurements. A conclusion is that the radial profile of floating potential is unsuitable for inferring the azimuthal $\boldsymbol{E} \times \boldsymbol{B}$-drift profile.

In LAPD-U, the region of $\boldsymbol{E} \times \boldsymbol{B}$-drift centered on the cylindrical axis was bounded at small radius by the criterion of electrode-disc bias equal to the space potential of the plasma. For radii smaller than this boundary's radius, insignificant space-potential drop was measured and no azimuthal ion drift was measured with the Mach probe. For radii larger than this boundary's radius, the space-potential drop was significant and the expected values of $\boldsymbol{E} \times \boldsymbol{B}$ drift speed were measured with the Mach probe. The off-axis current channel was located within this $\boldsymbol{E} \times \boldsymbol{B}$ drift region.

Although the time-stationary structure observed in the density perturbation has characteristics that are consistent with the StIA model, additional details are being acquired. A more thorough comparison between laboratory experiments and analytical theory will be the subject of a separate paper.

6. Conclusions

A terminating spiral electrode produced a controllable, parabolic radial profile of floating potential in the Q-machine at West Virginia University. The space potential profile showed no such structure. Laser-induced fluorescence measurements confirmed that the azimuthal ion drift velocity is inconsistent with a drift due to a gradient in the space potential. Based on these results, a multi-segment disc electrode was designed and built for use in the LAPD-U at UCLA Sub-Alfvénic $E \times B$ flow in the LAPD-U was produced by this electrode. Launched Alfvén waves concentrate within a cylindrical channel of partial plasma-density depletion. When electron current, density depletion and cross-field convection are combined, time-stationary, self-excited, structure is apparent in the perturbed plasma quantities. Effort toward better connecting this phenomenon to the StIA wave [1, 6] is underway.

Acknowledgments

References

[1] Knudsen D J 1996 *J. Geophys. Res.* **101** 10761
[2] Maltsev Y P, Lyatsky W B and Lyatskaya A M 1977 *Planet. Space Sci.* **25** 53
[3] Mallinckrodt A J and Carlson C W 1978 *J. Geophys. Res.* **83** 1426
[4] Stasiewicz K 2005 *J. Geophys. Res.* **110** A03220
[5] Goertz C K and Boswell R W 1979 *J. Geophys. Res.* **84** 7239
[6] Finnegan S M, Koepke M E and Knudsen D J 2008 *Phys. Plasmas* at press
[7] Finnegan S M, Koepke M E and Knudsen D J 2008 *Plasma Phys. Control. Fusion* at press
[8] Koepke M E 2007 *Rev. Geophys.* submitted
[9] Carroll III J J, Koepke M E, Zintl M W and Gavrishchaka V 2003 *Nonlinear Process. Geophys.* **10** 131
[10] Gekelman W, Pfister H, Lucky Z, Bamber J, Leneman D and Maggs J 1991 *Rev. Sci. Instrum.* **62** 2875
[11] Borovsky J E 1993 *J. Geophys. Res.* **98** 6101
[12] Chaston C C, Carlson C W, McFadden J P, Ergun R E and Strangeway R J 2007 *Geophys. Res. Lett.* **34** L07101
[13] Knudsen D J 2001 *Space Sci. Rev.* **95** 501
[14] Hui C H and Seyler C E 1992 *J. Geophys. Res.* **97** 3953
[15] Kletzing C A 1994 *J. Geophys. Res.* **99** 11095
[16] Clark A E and Seyler C E 1999 *J. Geophys. Res.* **104** 17233
[17] Stasiewicz K *et al* 2000 *Space Sci. Rev.* **92** 423
[18] Rankin R, Lu J Y, Marchand R and Donovan E F 2004 *Phys. Plasmas* **11** 1268
[19] Samson J C, Cogger L L and Pao Q 1996 *J. Geophys. Res.* **101** 17373
[20] Hill D N, Fornaca S and Wickham M G 1983 *Rev. Sci. Instrum.* **54** 309
[21] Carroll J J III, Koepke M E, Amatucci W E, Sheridan T E and Alport M J 1994 *Rev. Sci. Intrum.* **65** 2991
[22] Jassby D L 1971 *Rev. Sci. Instrum* **42** 1355
[23] D'Angelo N, Pécseli H L and Petersen P I 1974 *J. Geophys. Res.* **79** 4747
[24] Koepke M E, Carroll III J J, Zintl M W, Selcher C A and Gavrischchaka V 1998 *Phys. Rev. Lett.* **80** 1441